

TRANSITIONS OF ZONAL FLOWS IN A TWO-LAYER QUASI-GEOSTROPHIC OCEAN MODEL

MICKAEL D. CHEKROUN, HENK DIJKSTRA, TAYLAN ŞENGÜL, AND SHOUHONG WANG

ABSTRACT. We consider a 2-layer quasi-geostrophic ocean model where the upper layer is forced by a steady Kolmogorov wind stress in a periodic channel domain, which allows to mathematically study the nonlinear development of the resulting flow. The model supports a steady parallel shear flow as a response to the wind stress. As the maximal velocity of the shear flow (equivalently the maximal amplitude of the wind forcing) exceeds a critical threshold, the zonal jet destabilizes due to baroclinic instability and we numerically demonstrate that a first transition occurs. We obtain reduced equations of the system using the formalism of dynamic transition theory and establish two scenarios which completely describe this first transition. The generic scenario is that a conjugate pair of modes loses stability and a Hopf bifurcation occurs as a result. Under an appropriate set of parameters describing related midlatitude oceanic flows, we show that this first transition is continuous: a supercritical Hopf bifurcation occurs and a stable time periodic solution bifurcates. We also investigate the case of double Hopf bifurcations which occur when four modes of the linear stability problem simultaneously destabilize the zonal jet. In this case we prove that, in the relevant parameter regime, the flow exhibits a continuous transition accompanied by a bifurcated attractor homeomorphic to S^3 . The topological structure of this attractor is analyzed in detail and is shown to depend on the system parameters. In particular, this attractor contains (stable or unstable) time-periodic solutions and a quasi-periodic solution.

CONTENTS

1. Introduction	1
2. The model	3
3. Results	5
3.1. Linear Stability Analysis	5
3.2. Hopf Bifurcation	9
3.3. Double Hopf Bifurcation	11
4. Summary and Discussion	13
Appendix A. Proof of Lemma 3.1 and Theorem 3.1	15
Appendix B. Proof of Lemma 3.2 and Theorem 3.2	16
Appendix C. Numerical treatment of the linear stability problem	18
Appendix D. Practical aspects for the calculation of the transition number	19
Appendix E. Model Parameters	20
Acknowledgments:	20
References	20

1. INTRODUCTION

Baroclinic instability is among the most important geophysical fluid dynamical instabilities playing a crucial role in the dynamics of atmospheres and oceans. In particular, this instability mechanism is the dominant process in atmospheric dynamics shaping the cyclones and anticyclones that dominate weather in mid-latitudes, as well as the mesoscale ocean eddies that play various roles in oceanic dynamics and the transport of heat and salt [36]. Much is known on the linear stability of zonal jets in a horizontally unbounded ocean in the quasi-geostrophic (QG) flow regime. Classical models, such as the continuously stratified Eady model [14] and the

two-layer Phillips model [27], have lead to a detailed understanding of the mechanism of baroclinic instability of a zonal jet in the inviscid case. Long waves destabilize the zonal jet with maximum growth rates occurring for perturbations having wavelengths on the order of the Rossby deformation radius, typically 50 – 100 km for the mid-latitude ocean [35].

In case linear friction is included in the two-layer model, the neutral curve has a minimum at (k_c, μ_c) where k_c is the critical wavenumber and μ_c the critical value of the control parameter (e.g. the maximum speed of the zonal jet). The nonlinear development of these perturbations has been extensively analyzed in the weakly nonlinear case [25, 28, 39, 18]. In the regime $|k - k_c| = \mathcal{O}(\epsilon)$ and $|\mu - \mu_c| = \mathcal{O}(\epsilon^2)$, [37] showed that on a long time scale $T = \epsilon^2 t$ and large spatial scale $X = \epsilon(x - c_g t)$, where c_g is the group velocity of the waves at criticality, the complex amplitude A of the wave packet destabilizing the jet satisfies a Ginzburg-Landau equation, written as

$$\frac{\partial A}{\partial T} = \gamma_1 A + \gamma_2 \frac{\partial^2 A}{\partial X^2} - \gamma_3 A |A|^2,$$

where the γ_i are complex constants. [37] also showed that the fixed point solution of this equation can become unstable to sideband instabilities. Subsequent analysis has shown [13] that upgradient momentum transport can occur due to the self-interaction of the instabilities leading to rectification of the zonal jet.

In reality, the ocean basins are zonally bounded by continents and the midlatitude zonal jets are part of the gyre system, for example the subpolar gyre and subtropical gyre in the North Atlantic, forced by the surface wind stress through Ekman pumping [26]. The problem of baroclinic instability of such non-parallel flows is much more complicated and has so far only been tackled numerically. When the wind-forced QG equations are discretized, the linear stability problem for the gyre flow results in a large-dimensional generalized eigenvalue problem, typically of dimension 10^4 . There are many results for the one-layer single- and double-gyre flows (for an overview, see [11, Chap. 5]), but in this case there is no baroclinic instability. There are relatively few results for the two-layer case. In [12], it was shown that in the two-layer case the double-gyre flow becomes unstable through a sequence of Hopf bifurcations. The perturbation flow patterns at criticality are “banana-shaped,” locally resembling those of baroclinic instability in the Philips model. Stable periodic orbits result from these Hopf bifurcations, typically given rise to meandering motion of the gyre boundary.

As an intermediate, more analytically tractable case, we consider here the baroclinic instability of a zonal jet for a two-layer QG model in a zonally periodic channel. In this case, the properties of the bounded geometry are somehow represented, as the patterns of the unstable modes are restricted by the periodicity of the channel, so a sequence of Hopf bifurcations is expected just as in the more realistic gyre case. In addition, parallel flow solutions exist in the zonally periodic channel which simplifies the linear stability problem substantially such that a more detailed nonlinear analysis, akin to that in the horizontally unbounded case, can be performed. The parallel flow can also be connected to the surface wind stress, as in the full gyre case, but at the expense of adding an additional linear friction term to the upper layer vorticity equation; for more details, see [Section 2](#) below. In this way, the situation studied is more relevant for the stability of the Antarctic Circumpolar Current, than for the midlatitude gyre circulations.

The case specifically studied in the paper is the circulation set up by a time-independent Kolmogorov wind-stress field (for $k = 1, 2, \dots$)

$$\tau^x(y) = -\tau \frac{\tau_0}{k\pi} \cos k\pi \frac{y}{L_y}; \quad \tau^y = 0$$

where τ_0 is a characteristic mid-latitude wind-stress value. This wind stress forces an ocean in a periodic channel $[0, \mathbb{R}/(2L_x\mathbb{Z})] \times [-L_y, L_y]$ on the β -plane. The case $k = 1$ and $k = 2$ are often referred to as the single- and double-gyre forcing. The stratification is modeled in terms of a two-layer system and the wind stress only directly forces the upper layer. As a response to this wind stress, the system supports a basic shear flow ψ^s . The amplitude τ that controls the wind-stress curl, or equivalently the maximal velocity of the shear flow ψ^s is chosen as the bifurcation parameter.

We first perform a numerical linear stability analysis of this basic shear flow; for small values of τ , all associated eigenvalues have negative real parts such that the jet is stable. When the aspect ratio of the channel $a = L_y/L_x$ is large, the eigenvalues remain in the left complex plane regardless of the value of τ . However, when the aspect ratio gets small, the basic shear flow loses stability at a critical τ in the form of a single conjugate pair or two conjugate pairs of eigenvalues crossing the imaginary axis, giving rise to either a Hopf or a double

Hopf bifurcation. We next use the idea and method of the dynamic transition theory [20, 21], which is aimed to determine all the local attractors near a transition. The approach allows for a classification near the instability onset of all transitions into three classes known as continuous, catastrophic and random types [21]. In this way, our study extends previous results using this approach on the single-layer barotropic case [32, 10], the two-layer case for constant zonal jet velocities [3] and the barotropic Munk western boundary layer current profile case [15], to the zonally periodically bounded two-layer case.

Using the center manifold reduction, we obtain effective reduced (ordinary differential equation, ODE) models describing this transition. The dynamic transition theory identifies then transition numbers that qualifies the transition's type and are calculated from the reduced ODE's coefficients. The case of a Hopf bifurcation is generic while the case of a double Hopf bifurcation is degenerate and requires fine tuning of the aspect ratio to critical values where two conjugate pairs of eigenmodes with consecutive wavenumbers have their eigenvalues crossing the imaginary axis simultaneously. Using standard parameter values describing the midlatitude related oceanic flows, we perform numerical computations of the transition number for the forcing patterns corresponding to $k = 1, 2, 3$ and the aspect ratios $a \geq 3$. We find that in the parameter regimes we are interested in, the Hopf bifurcation is supercritical and a stable limit cycle bifurcates. For the double Hopf bifurcation, we find that after the corresponding transition takes place, the system exhibits a bifurcated local attractor [20] near the basic shear flow which is homeomorphic to the 3D-sphere. The topological structure of this attractor is analyzed and depending on the parameters, it is found to contain a combination of limit cycles and a quasi periodic solution.

The paper is organized as follows. In Section 2, the quasi-geostrophic model is presented. This is followed by Section 3 where the theory and numerical results for the linear stability problem (Section 3.1), the Hopf bifurcation case (Section 3.2) and the double-Hopf bifurcation case (Section 3.3) are presented. These results are summarized and discussed in Section 4. Appendix A and Appendix B contains details regarding the proofs of the transition theorems and the explicit formulas of the corresponding reduced ODE's coefficients, in the Hopf and double-Hopf cases, respectively. Appendix C and Appendix D, as for them, provide details about for the numerical treatment of the linear stability analysis and the practical computation of the transition numbers. Finally the set of model parameters used in the numerical study of the problem is given in Appendix E.

2. THE MODEL

We consider two layers of homogeneous fluids, each with a different and constant density ρ_1 and ρ_2 and with equilibrium layer thicknesses H_1 and H_2 , on a mid-latitude β -plane with Coriolis parameter $f = f_0 + \beta_0 y$. The lighter fluid in layer 1 is assumed to lie on top of the heavier one in layer 2 so that the stratification is statically stable, i.e., $\rho_1 < \rho_2$; bottom topography is neglected.

This flow can be modeled by the two-layer QG model [25] using the geostrophic stream function ψ_i and the vertical component of the relative vorticity ζ_i in each layer ($i = 1, 2$). The quantities ψ_i and ζ_i are non-dimensionalised by UL_y and U/L_y , respectively, wind stress with τ_0 , length with L_y , and time with L_y/U , where U is a characteristic horizontal velocity. By choosing $U = \tau_0/(\rho_0\beta_0L_yH_1)$, where ρ_0 is a reference density, the dimensionless equations on the domain $(0, 2/a) \times (-1, 1)$ (with $a = L_y/L_x$) become

$$(2.1) \quad \begin{aligned} \left[\frac{\partial}{\partial t} + \{\psi_1, \cdot\} \right] (\Delta\psi_1 + F_1(\psi_2 - \psi_1) + \beta y) &= -r_1\Delta\psi_1 - \tau\beta \sin k\pi y \\ \left[\frac{\partial}{\partial t} + \{\psi_2, \cdot\} \right] (\Delta\psi_2 + F_2(\psi_1 - \psi_2) + \beta y) &= -r_2\Delta\psi_2, \end{aligned}$$

where $\{f, g\} = f_x g_y - f_y g_x$ is the usual Jacobian operator and

$$\mathcal{F}_1 = -r_1\Delta\psi_1,$$

represents the damping of upper layer vorticity due to frictional processes. In the bottom layer, we include a linear (Ekman) friction term $-r_2\Delta\psi_2$; in both layers, Laplacian friction terms are neglected due to the absence of continental boundary layers making such terms much smaller than the other ones. The expressions for the dimensional and dimensionless parameters, with their standard values at a latitude 45°N , are given in Table 2.

For the boundary conditions, we assume periodicity in the x -direction and free-slip boundaries in the y -direction. Hence, the conditions are

$$(2.2) \quad \begin{aligned} \psi_i|_{x=0} &= \psi_i|_{x=2/a}, & i &= 1, 2. \\ \psi_i|_{y=\pm 1} &= \frac{\partial^2 \psi_i}{\partial y^2}|_{y=\pm 1} = 0, & i &= 1, 2. \end{aligned}$$

In actual ocean basins, a steady zonal jet is generated by the applied wind stress through Ekman pumping, a Sverdrup balance and a western boundary layer flow [26]. Due to the periodic boundary conditions used here, such a flow cannot be captured in this model. However, due to the presence of the large upper layer friction, which corrects for the absence of the Sverdrup balance, the equations allow a steady state of the form

$$(2.3) \quad \psi_1^s = \Psi \sin k\pi y, \quad \psi_2^s = 0,$$

which relates to the wind stress field, when $\mathcal{F}_1 - \tau\beta \sin k\pi y = 0$. In this paper, we will assume that the wind-stress vorticity input is balanced by vorticity decay due to the linear friction term $\mathcal{F}_1 = -r_1 \Delta \psi_1$, being aware that a larger friction coefficient r_1 is needed than can be justified from existing dissipative processes in the ocean. In this case, it follows that

$$(2.4) \quad \Psi = \frac{\tau\beta}{(k\pi)^2 r_1}.$$

The parameter Ψ appearing in (2.3) can then be chosen as the control parameter as is the case in this study, instead of τ . It can be interpreted as the maximal (zonal) velocity of the shear flow (after taking the derivative in y of (2.3)) or equivalently the maximal amplitude of the wind forcing according to (2.4).

By considering the perturbation $\psi'_i = \psi_i - \psi_i^s$, $i = 1, 2$, we can write the system into the following operator form (after dropping the prime notation)

$$(2.5) \quad \mathcal{M} \partial_t \psi = \mathcal{N} \psi + \mathcal{G}(\psi), \quad \psi = (\psi_1, \psi_2),$$

where \mathcal{M} and \mathcal{N} are the linear operators defined as

$$(2.6) \quad \mathcal{M} \psi = \begin{bmatrix} \Delta \psi_1 + F_1(\psi_2 - \psi_1) \\ \Delta \psi_2 + F_2(\psi_1 - \psi_2) \end{bmatrix},$$

and

$$(2.7) \quad \mathcal{N} \psi = \begin{bmatrix} \Psi k\pi \cos k\pi y \left((k\pi)^2 \frac{\partial \psi_1}{\partial x} + F_1 \frac{\partial \psi_2}{\partial x} + \frac{\partial \Delta \psi_1}{\partial x} \right) - \beta \frac{\partial \psi_1}{\partial x} - r_1 \Delta \psi_1 \\ -\Psi k\pi F_2 \cos k\pi y \frac{\partial \psi_2}{\partial x} - \beta \frac{\partial \psi_2}{\partial x} - r_2 \Delta \psi_2 \end{bmatrix}.$$

Lastly, the bilinear nonlinearity is given explicitly by

$$(2.8) \quad \mathcal{G}(\psi) = \begin{bmatrix} -\{\psi_1, \Delta \psi_1 + F_1(\psi_2 - \psi_1)\} \\ -\{\psi_2, \Delta \psi_2 + F_2(\psi_1 - \psi_2)\} \end{bmatrix}.$$

The operators \mathcal{G} and \mathcal{N} are well-defined mappings, $\mathcal{G} : H_1 \rightarrow H_{-1}$ and $\mathcal{N} : H_0 \rightarrow H_{-1}$, on the following functional spaces:

$$(2.9) \quad \begin{aligned} H_1 &= \{\psi = (\psi_1, \psi_2) \in H^4(\Omega) \times H^4(\Omega) \mid \psi \text{ satisfies (2.2)}\}, \\ H_0 &= \{\psi = (\psi_1, \psi_2) \in H^2(\Omega) \times H^2(\Omega) \mid \psi \text{ satisfies (2.2)}\}, \\ H_{-1} &= L^2(\Omega)^2. \end{aligned}$$

Here,

$$(2.10) \quad \Omega = (0, 2/a) \times (-1, 1), \text{ with } a = L_y/L_x,$$

and $H^4(\Omega)$, $H^2(\Omega)$, $L^2(\Omega)$ are the usual Sobolev and Lebesgue function spaces endowed with their natural inner products. These functional spaces account for spatial regularity of the solution ψ for which $H^p(\Omega)$ denotes the space of square-integrable functions that possess p th-order derivatives (in the distribution sense) that are

themselves square-integrable; see e.g. [2]. Using this functional framework, it can be shown that Eq. (2.5) is well-posed by application of e.g. a standard approximation method (such as Galerkin) [1].

3. RESULTS

In this section, we first present the linear stability analysis of the basic shear flow and then we move on to describe the first transitions due to the instabilities, covering both the Hopf and double Hopf bifurcations. Although in realistic ocean basins the aspect ratio a would be small, we allow here the full range of a to also study the nonlinear interactions of localized instabilities.

3.1. Linear Stability Analysis. We first investigate the linear stability of the basic solution. For this purpose, we denote the eigenmodes of the linear problem by

$$\psi_{m,j}(x, y) = e^{i\alpha_m x} Y_j(y), \quad j \in \mathbb{N}, m \in \mathbb{Z}, \quad \alpha_m = am\pi.$$

with eigenvalues $\sigma_{m,j}$, i.e.

$$(3.1) \quad \sigma_{m,j} \mathcal{M} \psi_{m,j} = \mathcal{N} \psi_{m,j}.$$

Since the linear operators \mathcal{M} and \mathcal{N} are real, we have

$$\overline{\sigma_{m,j}} = \sigma_{-m,j}, \quad \overline{\psi_{m,j}} = \psi_{-m,j}, \quad \forall m \in \mathbb{N}.$$

This eigenvalue problem is solved numerically by means of a standard Legendre-Galerkin method; see Appendix C. A typical picture of the spectrum near the criticality is given in Figure 1. This figure shows that many eigenvalues are clustered near the imaginary axis at the critical parameter value $\Psi = \Psi_c$ as defined in (3.3) below.

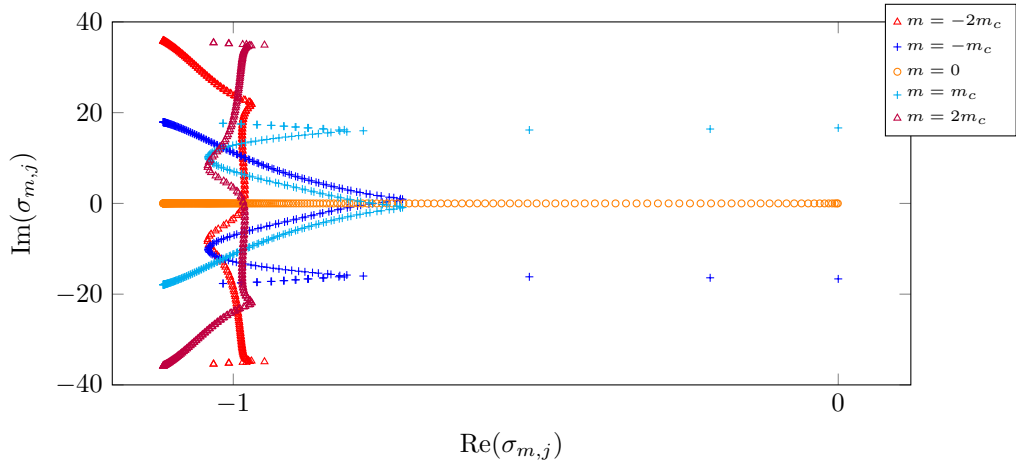


FIGURE 1. The first 240 eigenvalues at the critical parameter when $m_c = 2$, $a = 10$, $k = 1$ and $N_y = 240$.

We assume (as confirmed numerically for the parameter regimes considered below) that the eigenvalues are ordered so that for each integer m , $\sigma_{m,1}$ has the largest real part among the $\sigma_{m,j}$, for any nonnegative integer j .

For each (nonnegative) wavenumber m , we define Ψ_m , when it exists, to be the value of Ψ for which the eigenvalue $\sigma_{m,1}$ crosses the imaginary axis, that is

$$(3.2) \quad \text{Re}(\sigma_{m,1}) = \text{Re}(\sigma_{-m,1}) = \begin{cases} < 0, & \text{if } \Psi < \Psi_m \\ = 0, & \text{if } \Psi = \Psi_m \\ > 0, & \text{if } \Psi > \Psi_m \end{cases}.$$

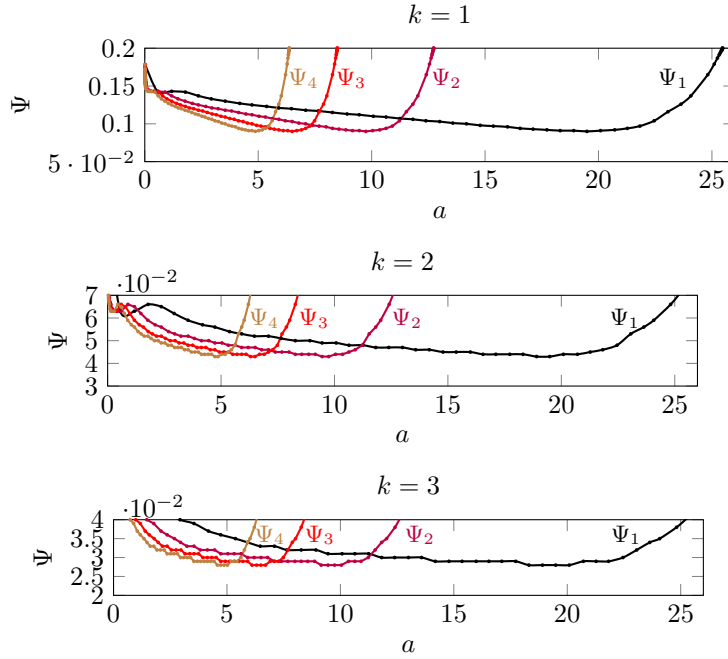


FIGURE 2. Neutral stability curves Ψ_m , $m = 1, 2, 3, 4$ defined in (3.2), for wind-stress profiles defined by $k = 1, 2, 3$. For values of $\Psi > \Psi_m$, the shear flow (ψ_1^s, ψ_2^s) in (2.3) becomes unstable to a perturbation pattern with wavenumber α_m .

Hence $\Psi = \Psi_m$ defines a neutral stability curve in the (a, Ψ) -plane. In Figure 2, these neutral curves are plotted for zonal wave numbers $m = 1, 2, 3, 4$.

Our numerical analysis suggests that for any m , Ψ_m is well-defined only for aspect ratios of the basin characteristic lengths smaller than a threshold a_m (depending on m), that is for $a < a_m$. The threshold a_m is defined by a vertical asymptote condition, namely

$$\lim_{a \rightarrow a_m^-} \Psi_m = \infty.$$

Moreover, we numerically observe that the a_m are ordered such that

$$\infty > a_1 > a_2 > \dots$$

We define then the **critical maximal shear flow's velocity**, Ψ_c , and the critical zonal wavenumber, m_c , by

$$(3.3) \quad \Psi_c = \min_{m \in \mathbb{N}} \Psi_m,$$

and,

$$(3.4) \quad m_c = \operatorname{argmin}_{m \in \mathbb{N}} \Psi_m,$$

respectively.

A typical structure of the spectrum at the critical parameter value, $\Psi = \Psi_c$, is shown in Figure 1 where a conjugate pair of eigenvalues is about to cross the imaginary axis. The eigenvalues on the real axis correspond to the wavenumber $m = 0$ and are always stable although they may be very close to zero as shown in Figure 1.

To describe the solutions near the onset of transition $\Psi = \Psi_c$, we define the spatio-temporal function

$$(3.5) \quad f_m(x, y, t) = 2 \operatorname{Re} \left(e^{i \operatorname{Im}(\sigma_{m,1})t} \psi_{m,1}(x, y) \right), \quad m \in \mathbb{Z},$$

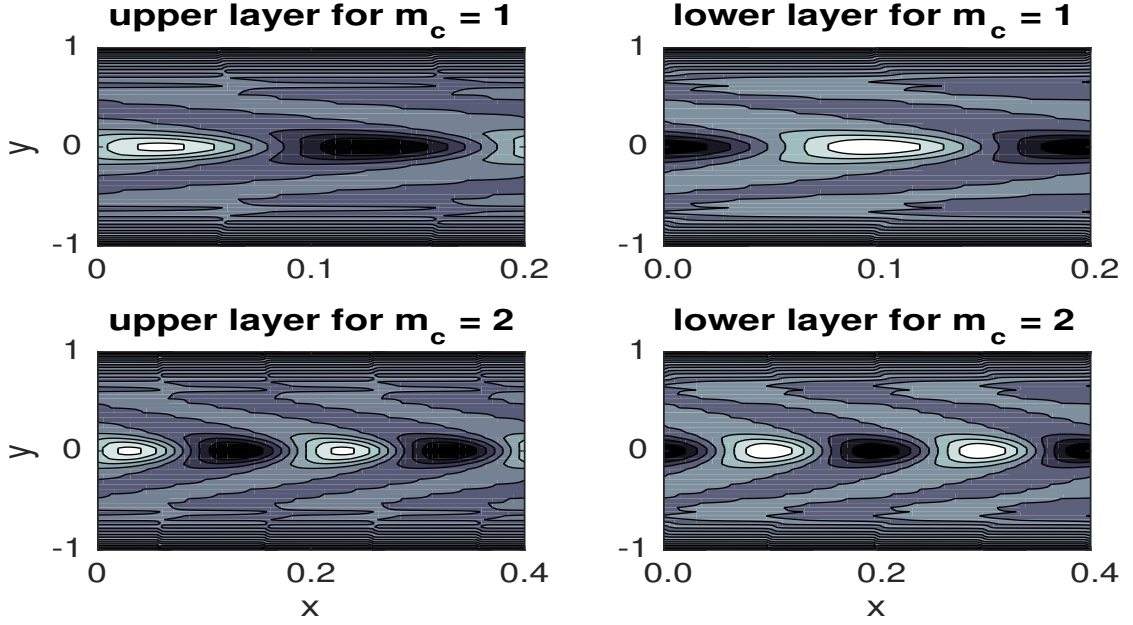


FIGURE 3. Real part of the upper and lower layers of the time-periodic solution f_{m_c} (or equivalently of the dominant eigenmode $\psi_{m_c,1}$) at $t = 0$ for $k = 1$ and $a = 10$ and $a = 5$, respectively.

where $\sigma_{m,1}$ is the first eigenvalue and $\psi_{m,1}$ is its associated eigenfunction. The spatial structure of the eigenmodes $\psi_{m_c,1}$ is shown in [Figure 3](#), revealing the well-known “banana-shaped” patterns characteristics of baroclinic instability.

The values of Ψ_c with respect to the aspect ratio a for $k = 1, 2, 3$ is shown in [Figure 4](#). By the previous remarks,

$$(3.6) \quad \lim_{a \rightarrow a_1^-} \Psi_c = \lim_{a \rightarrow a_1^-} \Psi_1 = \infty.$$

By (3.6), for $a > a_1$, the system is linearly stable. As is expected, the neutral stability curves ([Figure 2](#)) approach the asymptote $\Psi_c \rightarrow \infty$ as a converges to the critical aspect ratio a_1 over which the system is linearly stable for all Ψ . Our numerical results in [Figure 4](#) show that for aspect ratios a in the range $3 \leq a \leq 20$, the critical maximal shear velocity $\Psi_c \approx 0.1, 0.04, 0.03$ for $k = 1, 2, 3$ respectively. By (2.4), this value of critical maximal shear velocity corresponds to an upper layer friction that is approximately,

$$r_1 \approx \frac{\tau\beta}{k^2\pi^2\Psi_c} \approx \frac{10^3}{k},$$

which is indeed much larger than can be justified from dissipative processes in the ocean but, as explained in [Section 2](#), is needed here to connect the background zonal jet to the applied wind stress as a Sverdrup balance is absent in the original model formulation.

The friction term in the lower layer however is physical (Ekman friction) and for this study, it is fixed at $r_2 = 5.0$, see [Table 2](#). Also, from [Figure 2](#), we see that for small aspect ratios, many modes become unstable as Ψ_c is exceeded.

For $a < a_1$, the system has a first transition at $\Psi = \Psi_c$ and exactly one of the following two principal of exchange of stability (PES) condition holds:

$$(3.7) \quad \begin{aligned} Re(\sigma_{m,1}) = Re(\sigma_{-m,1}) & \begin{cases} < 0, & \text{if } \Psi < \Psi_c \\ = 0, & \text{if } \Psi = \Psi_c \\ > 0, & \text{if } \Psi > \Psi_c \end{cases} & \text{if } m = m_c \\ Re(\sigma_{m,1}) = Re(\sigma_{-m,1}) < 0 & & \text{if } m \neq m_c \end{aligned}$$

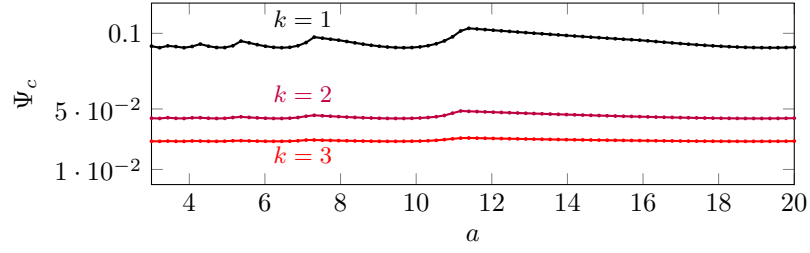


FIGURE 4. The critical maximal shear flow's velocity Ψ_c dependence on the channel's aspect ratio a for $k = 1, 2$ and $k = 3$.

k	m_c	a_{DH}	Ψ_c	$Re(A)$	$Re(B)$	$Re(C)$	$Re(D)$	δ	θ	$\delta\theta$
1	1	11.26	0.10	-0.25	-1.00	0.01	-0.33	-0.05	3.08	-0.15
1	2	7.30	0.10	-0.37	-1.00	-0.13	-0.40	0.36	2.51	0.89
1	3	5.38	0.10	-0.95	-1.00	-0.22	-0.61	0.23	1.65	0.37
1	4	4.23	0.09	-0.81	-1.00	-0.29	-0.61	0.36	1.63	0.58
2	1	11.18	0.05	-0.15	-1.00	0.12	-0.23	-0.77	4.39	-3.38
2	2	7.20	0.05	-0.34	-1.00	-0.04	-0.46	0.13	2.20	0.28
2	3	5.27	0.05	-0.37	-1.00	-0.14	-0.45	0.38	2.24	0.86
2	4	4.14	0.05	-0.38	-1.00	-0.21	-0.44	0.55	2.25	1.25

TABLE 1. The double Hopf transition numbers. Here $k = 1, 2$ is the wavenumber of the forcing, m_c and $m_c + 1$ are the wavenumbers of the first two critical modes which become unstable simultaneously at the critical aspect ratio a_{DH} . A, B, C, D are the coefficients of the double Hopf transition normalized with respect to the maximum absolute value of those coefficients. The parameters δ and θ are defined by (3.14).

$$(3.8) \quad \begin{aligned} Re(\sigma_{m,1}) = Re(\sigma_{-m,1}) & \begin{cases} < 0, & \text{if } \Psi < \Psi_c \\ = 0, & \text{if } \Psi = \Psi_c \\ > 0, & \text{if } \Psi > \Psi_c \end{cases} & \text{if } m \in \{m_c, m_c + 1\} \\ Re(\sigma_{m,1}) = Re(\sigma_{-m,1}) < 0 & & \text{if } m \notin \{m_c, m_c + 1\}. \end{aligned}$$

According to (3.7) and (3.8) either, two or four eigenvalues become unstable as Ψ crosses Ψ_c . The case of two critical eigenvalues is generic and results into a Hopf bifurcation. The case of four critical eigenvalues results in a double Hopf bifurcation and requires the fine-tuning of the aspect ratio $a = a_{DH}$ so that $\Psi_c = \Psi_{m_c} = \Psi_{m_c+1}$. The values of a_{DH} where double Hopf transition occurs is given in Table 1.

Although the double Hopf transition is not generic, its analysis gives an insight into regimes of moderate values of Ψ where multiple eigenvalues are unstable. In Figure 5, we show the dominant part of the spectrum of the linearized operator at a critical aspect ratio a_{DH} .

We recall that the neutral stability curves (shown in Figure 2) are found by identifying the set of parameter values (here in the (a, Ψ) -plane) for which the real part of the critical eigenvalue is zero while the rest of the eigenvalues have a negative real part, i.e. are associated with a stable mode. By a continuity argument, we can thus infer that in a neighborhood of such critical curves the PES condition is satisfied, for instance when Ψ crosses the critical value Ψ_c (depending on a and k) shown in Figure 2.

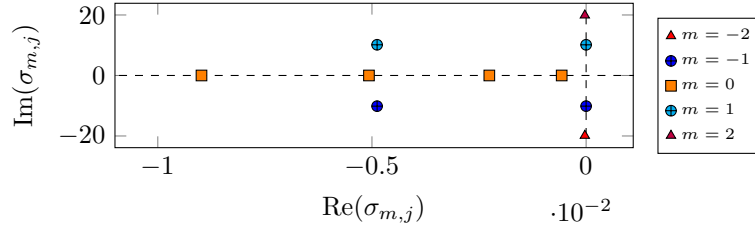


FIGURE 5. The spectrum near the double Hopf aspect ratio $a_{DH} = 11.263$ for $k = 1$. The first four critical eigenvalues $\sigma_{m,1}$, m in $\{-2, -1, 1, 2\}$, can be seen on the imaginary axis.

The PES condition (3.7) has been rigorously verified for Kolmogorov flows in [22] via a continued fraction method. This method has later been extended for the single layer QG model for the $k = 1$ case in [32] and for $k \geq 2$ in [19] where k is the forcing frequency in (2.1). It is still an open problem to rigorously verify the PES condition for the current problem.

3.2. Hopf Bifurcation. We first investigate the generic Hopf transition scenario based on the attractor bifurcation theorem [20, Theorem 5.2] and the dynamical transition theorem [21, Theorem 2.1.3]. For proofs of the following lemma and theorem, see Appendix A).

Lemma 3.1. *Assume that the PES condition (3.7) holds. Then the transition and stability of the steady state solution (2.3) to Eq. (2.5), in the vicinity of the critical maximal shear flow's velocity $\Psi = \Psi_c$ and for any sufficiently small initial data, are equivalent to the stability of the zero solution of the following reduced equation*

$$(3.9) \quad \frac{dz}{dt} = \sigma_{m_c,1}z + Pz|z|^2 + o(|z|^3),$$

where $z(t)$ denotes the complex amplitude aiming at approximating the projection of the model's solution onto the critical mode $\psi_{m_c,1}$. The coefficient P is defined in Eq. (A.8) of Appendix A and is called the **transition number**.

The analysis of Lemma 3.1 yields the following theorem.

Theorem 3.1. *Assume that the first critical eigenvalue is purely complex with a simple multiplicity, that is the PES condition (3.7) is satisfied. Then the following assertions hold true.*

- (1) *If $\text{Re}(P) < 0$, then Eq. (2.5) in H_1 (see (2.9)) undergoes a continuous transition accompanied by a supercritical Hopf bifurcation on $\Psi > \Psi_c$, with Ψ_c defined in (3.3). In particular, the steady-state solution bifurcates to a stable periodic solution ψ on $\Psi > \Psi_c$, satisfying $\psi \rightarrow \mathbf{0}$ as $\Psi \rightarrow \Psi_c$ and has the following approximation*

$$(3.10) \quad \psi(x, y, t) = \left(\frac{-\text{Re}(\sigma_{m_c,1})}{\text{Re}(P)} \right)^{\frac{1}{2}} f_{m_c}(x, y, t) + o\left(|\Psi - \Psi_c|^{\frac{1}{2}}\right).$$

The spatial structure of the time periodic solution ψ is shown at $t = 0$ for different aspect ratios a in Figure 3.

- (2) *If $\text{Re}(P) > 0$, then Eq. (2.5) in H_1 (see (2.9)) undergoes a jump transition on $\Psi < \Psi_c$ accompanied by a subcritical Hopf bifurcation. In particular, an unstable periodic solution ψ given by (3.10) bifurcates on $\Psi < \Psi_c$ and there is no periodic solution bifurcating from $\mathbf{0}$ on $\Psi > \Psi_c$. Moreover, there is a singularity separation at some $\Psi_s < \Psi_c$ generating an attractor and an unstable periodic solution ψ .*

When the PES condition (3.7) holds, the system exhibits a Hopf bifurcation as described by Theorem 3.1. The type of transition boils down to the determination of the transition number P given in (A.8) of Appendix A. For the practical calculation of this number, we refer to Appendix D. A numerical evaluation of P as reported in Figure 6 shows that for a low-frequency forcing ($k = 1, 2, 3$), generally $\text{Re}(P) < 0$ and as a result *only continuous transition (supercritical Hopf bifurcation) is possible for the parameter regime we have selected*. In Figure 6, we also display the critical wavenumber m_c . In the range $4 \leq a \leq 20$, the critical wavenumber m_c is found to range from 1 to 4.

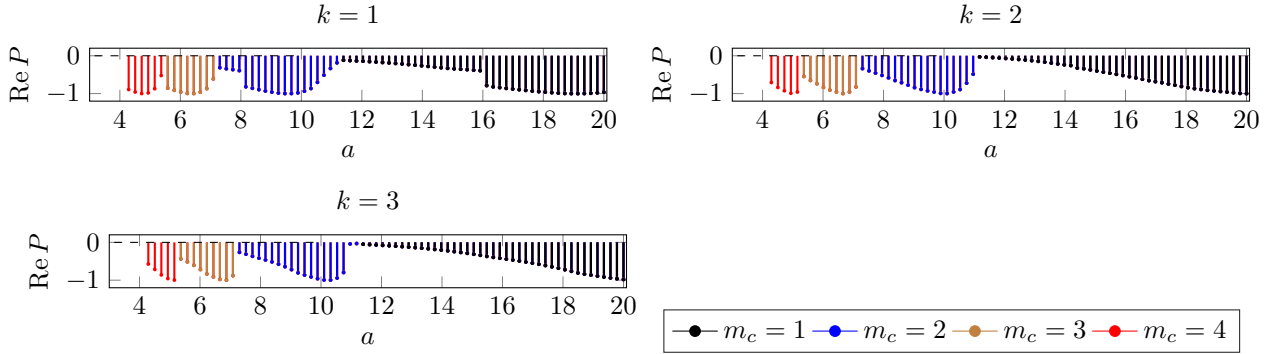


FIGURE 6. The real part of the transition number P compared to the channel aspect ratio a normalized by the largest absolute value of $\text{Re } P$. The parameters are as set in [Table 2](#).

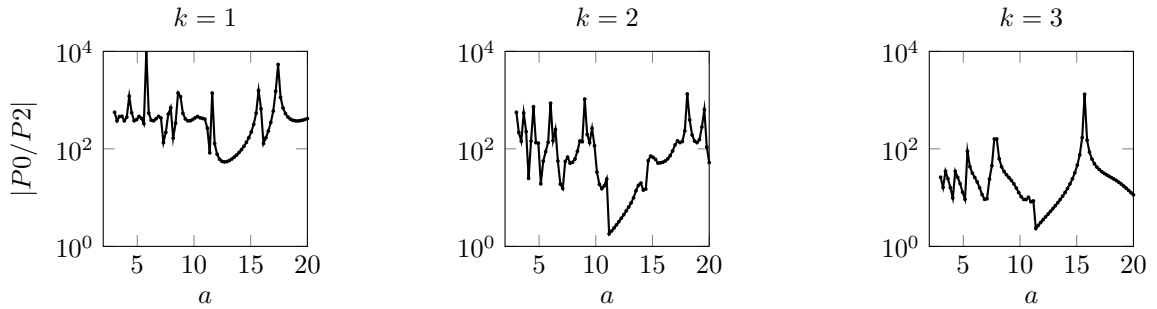


FIGURE 7. The effect of P_0 (of $m = 0$ modes) compared to the effect P_2 (of $2m_c$ modes) on the transition number.

There are discontinuities in P vs a plot in [Figure 6](#) of the transition number which are due to the changes in the critical zonal wavenumber m_c . These discontinuities take place at double Hopf bifurcation aspect ratios where two consecutive zonal wavenumbers become critical simultaneously which is investigated in the next section. However, there are also discontinuities in [Figure 6](#), $k = 1$ case (for example near $a = 16$) whose origin is mysterious.

As detailed in [Appendix A](#), the transition number P accounts for two types of nonlinear interactions between the eigenmodes, and is written

$$P = P_0 + P_2,$$

where P_0 accounts for nonlinear interactions between the critical modes and the zonally homogeneous (stable) modes $m = 0$ (see [\(A.9\)](#) below), while P_2 accounts for the interactions between the critical modes and the modes having a wavenumber twice that of the critical modes (see [\(A.10\)](#) below). A comparison of typical numerical values of P_0 and P_2 shows that P_2 is several orders of magnitudes smaller than P_0 ; see [Figure 7](#). We refer to [[4](#), Theorem III.1] for a similar transition number diagnosing also the type of Hopf bifurcations arising, generically, in delay differential equations, and whose nature is also characterized by the interactions of linearized modes through the model's non-linear terms.

In our case,

$$P_0 = \sum_{j=0}^{\infty} P_{0,j}$$

where $P_{0,j}$ measures the contribution to P of the j -th mode with zero-wavenumber ($m = 0$) interacting with the critical mode; see [\(A.9\)](#) again. [Figure 8](#) shows that the dependence of $P_{0,j}$ on j is essentially linear. We believe the results in [Figure 7](#) and [Figure 8](#) may help when choosing the modes to include in a simulation when the maximal shear velocity is well above the criticality.

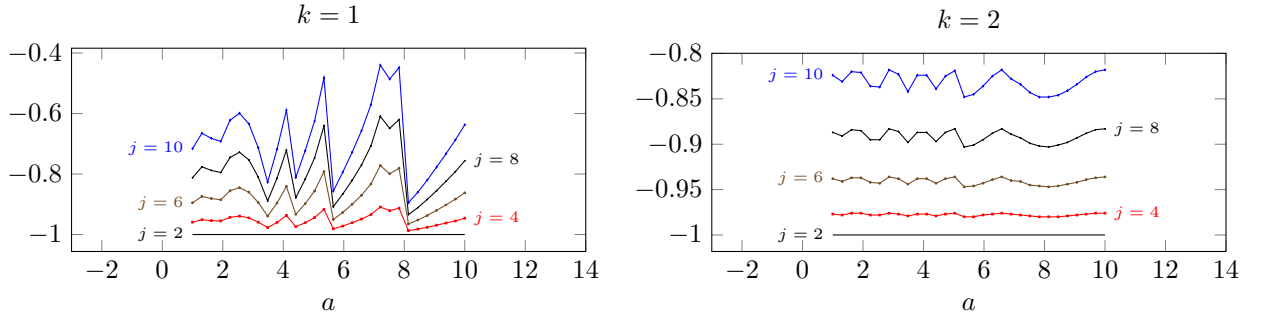


FIGURE 8. $P_{0,j}/|P_{0,2}|$ for even values of j . $P_{0,j} = 0$ for odd values of j .

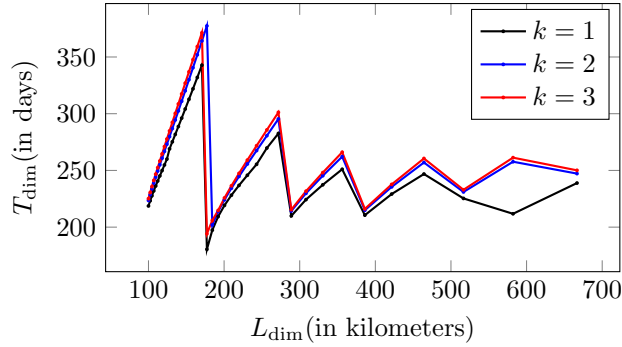


FIGURE 9. The (dimensional) time period $T_{\text{dim}} = \frac{2\pi}{\text{Im}(\sigma_{m_c,1})} \frac{L_y}{U}$ compared to the (dimensional) length of the channel $L_{\text{dim}} = 2L_y/a$ of the both stable and unstable bifurcated time periodic solution (3.10) in the Hopf bifurcation case. Here L_y and U are the characteristic scales defined in Table 2. The jumps in the derivative of the time period of the bifurcated solution is due to the change of the imaginary part $\text{Im} \sigma_{m_c,1}$ of the critical eigenvalue at the double Hopf aspect ratios a_{DH} .

We also compare the dimensional time period of the bifurcated solution (3.10) to the (dimensional) length of the channel in Figure 9. With the default parameters as chosen in Table 2, our simulations yield a solution with time period of 180-380 days depending on the channel length of 100-700kms.

3.3. Double Hopf Bifurcation. In this section we are interested in the transitions that take place at the critical aspect ratios a_{DH} where four modes with consecutive wavenumbers $m_c, m_c + 1$ become unstable as given by the PES condition (3.8).

We first present the reduced equations in this case (for proofs, see Appendix B).

Lemma 3.2. *Assume that the PES condition (3.8) holds. Then, the transition and stability of the steady state solution (2.3) of Eq. (2.5) in H_1 (see (2.9)), in the vicinity of the critical zonal shear flow's velocity, $\Psi = \Psi_c$, and for any sufficiently small initial data are equivalent to the stability of the zero solution of the following system*

$$(3.11) \quad \begin{aligned} \frac{dz_1}{dt} &= \sigma_{m_c,1} z_1 + z_1(A|z_1|^2 + B|z_2|^2) + o(|z|^3), \\ \frac{dz_2}{dt} &= \sigma_{m_c+1,1} z_2 + z_2(C|z_1|^2 + D|z_2|^2) + o(|z|^3), \end{aligned}$$

where $z_1(t)$ and $z_2(t)$ denote the complex amplitudes aiming at approximating the projection of the model's solution onto the critical modes $\psi_{m_c,1}$ and $\psi_{m_c+1,1}$, respectively.

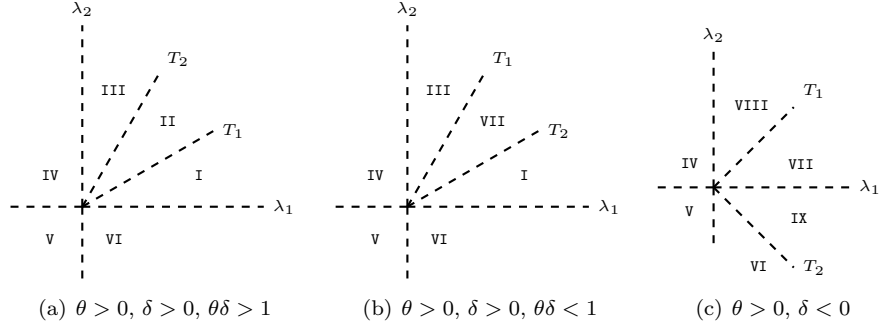


FIGURE 10. The regions in the λ_1 - λ_2 plane with different dynamical behaviors. In region V, the basic steady state is locally asymptotically stable. In regions IV and VI, the system undergoes a supercritical Hopf bifurcation. The dynamics in regions I, II and III is the double Hopf bifurcation scenario and the details are given in Figure 11. The lines T_1 and T_2 in the figure have slopes $1/\theta$ and δ (as defined in (3.14)) respectively.

The **transition numbers** A, B, C, D are determined by the nonlinear interactions of these critical modes with higher modes given by (B.2). More precisely, the terms A and D account for the self-interactions among the critical modes, while the terms B and C account for the cross-interactions between the critical modes with the higher modes.

It is known that the equation (3.11) exhibit a zoo of dynamical behaviors. We refer to [16] for a detailed analysis of all possible cases. Here, we restrict our attention to the case

$$(3.12) \quad \operatorname{Re}(A) < 0, \operatorname{Re}(B) < 0, \operatorname{Re}(B) + \operatorname{Re}(C) < 0, \operatorname{Re}(D) < 0,$$

which is the only case we observe in our numerical experiments, see Table 1. Under these conditions it is known that the transition is continuous (see Theorem 2.3 in [17]). For the next theorem, let us define the numbers

$$(3.13) \quad \lambda_1 = \operatorname{Re}(\sigma_{m_c,1}), \quad \lambda_2 = \operatorname{Re}(\sigma_{m_c+1,1}).$$

$$(3.14) \quad \delta = \frac{\operatorname{Re}(C)}{\operatorname{Re}(A)}, \quad \theta = \frac{\operatorname{Re}(B)}{\operatorname{Re}(D)}$$

$$\eta_1 = \left(\frac{\lambda_1 - \theta\lambda_2}{(\theta\delta - 1)\operatorname{Re}(A)} \right)^{\frac{1}{2}}, \quad \eta_2 = \left(\frac{\lambda_2 - \delta\lambda_1}{(\theta\delta - 1)\operatorname{Re}(D)} \right)^{\frac{1}{2}}.$$

Recalling f_{m_c} defined in (3.5) (with $m = m_c$), we define the following spatio-temporal profiles

$$(3.15) \quad \begin{aligned} \psi_p^{m_c}(x, y, t) &= \left(-\frac{\lambda_1}{\operatorname{Re}(A)} \right)^{\frac{1}{2}} f_{m_c}(x, y, t) + o\left(|\Psi - \Psi_c|^{\frac{1}{2}}\right), \\ \psi_p^{m_c+1}(x, y, t) &= \left(\frac{\lambda_2}{\operatorname{Re}(D)} \right)^{\frac{1}{2}} f_{m_c+1}(x, y, t) + o\left(|\Psi - \Psi_c|^{\frac{1}{2}}\right), \\ \psi_{qp}(x, y, t) &= \eta_1 f_{m_c}(x, y, t) + \eta_2 f_{m_c+1}(x, y, t) + o\left(|\Psi - \Psi_c|^{\frac{1}{2}}\right) \end{aligned}$$

Theorem 3.2. Assume that the conditions of Lemma 3.2 as well as the condition (3.12) hold. Then the equations (2.5) undergo a continuous transition at $\Psi = \Psi_c$, and an S^3 attractor Σ bifurcates on $\Psi > \Psi_c$, which converges to $\mathbf{0}$ as Ψ approaches to Ψ_c from right. Depending on the values of θ and δ , there are three transition scenarios as shown in Figure 10. In each scenario, near the onset of transition $(\lambda_1, \lambda_2) = (0, 0)$, the $\lambda_1 - \lambda_2$ plane is dissected into several regions with distinct topological structures for the attractor Σ as given in Figure 11.

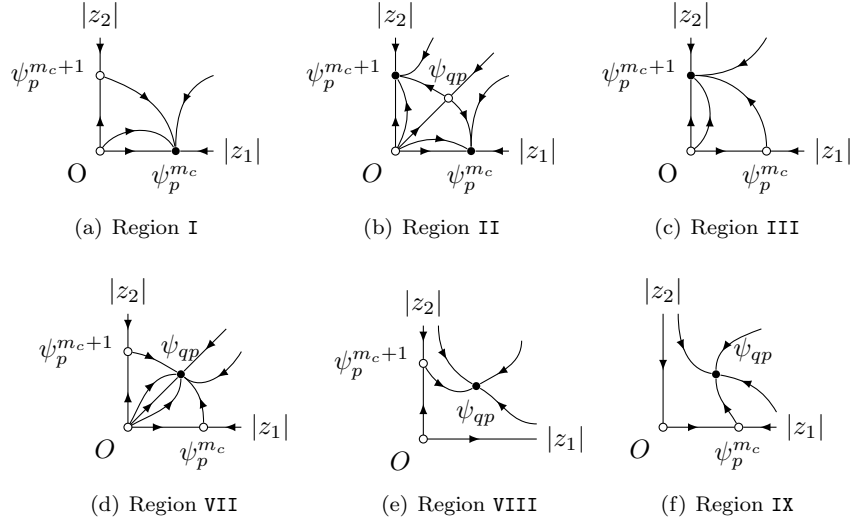


FIGURE 11. The dynamics in the regions given in the first quadrant of Figure 10. $\psi_p^{m_c}$, $\psi_p^{m_c+1}$ are time-periodic with zonal wavenumbers m_c and $m_c + 1$ respectively. ψ_{qp} is the quasiperiodic solution given in (3.15).

Remark 3.1. (1) If $z_2 = 0$ or $z_1 = 0$, the equations (3.11) reduce to the equation (3.9) with $A = P$ or $D = P$ respectively. Thus Lemma 3.1 and Theorem 3.1 are special cases of Lemma 3.2 and Theorem 3.2 respectively.

(2) We note that the features of the spatial structures of upper vs lower layer of the bifurcated periodic solutions in Figure 3 and the quasi-periodic solution in Figure 12 do not alter much. We expect that the situation would be different if bottom topography is included.

The transition scenario of double Hopf transition is given by Theorem 3.2 by Figure 10 and Figure 11. We find that near the onset of transition, depending on the fluctuations the basic state experiences a transition either to a time periodic solution or to a quasi periodic solution. Our results in Table 1 show that the three scenarios sketched in Figure 10 are realizable.

In particular, near a double Hopf transition point, one of the following three possibilities must occur post transition, $\Psi > \Psi_c$:

- (i) there is only a single stable limit cycle,
- (ii) there are two distinct stable limit cycles, and an unstable quasi-periodic solution
- (iii) there is a stable quasi-periodic solution and either one or two unstable limit cycles.

For the double Hopf transition, Theorem 3.2 basically tells that all of the above local structures, the time-periodic solution and the 2D torus, if they exist, reside in a local attractor homeomorphic to the three dimensional sphere. The existence of this attracting 3D sphere is guaranteed by the attractor bifurcation theorem; see [20, Theorem 6.1].

4. SUMMARY AND DISCUSSION

In this paper, we investigated the stability of a parallel zonal jet forced by a Kolmogorov-type wind stress in a periodic zonal channel, using a two-layer quasi-geostrophic (QG) model. This problem is, in terms of complexity, situated between the horizontally unbounded problem [27, 37] and the fully bounded gyre problem [12]. More precisely, the effect of boundaries is captured by the interactions of only a few modes (solutions of the linear stability problem), while still keeping a parallel flow which is connected to the wind-stress field.

Our results show, in the continuity of earlier works [15, 3, 10, 19], that the zonal shear flow is linearly stable if its maximal amplitude Ψ , or equivalently the maximal amplitude τ of the wind-stress curl (see (2.4)), is below

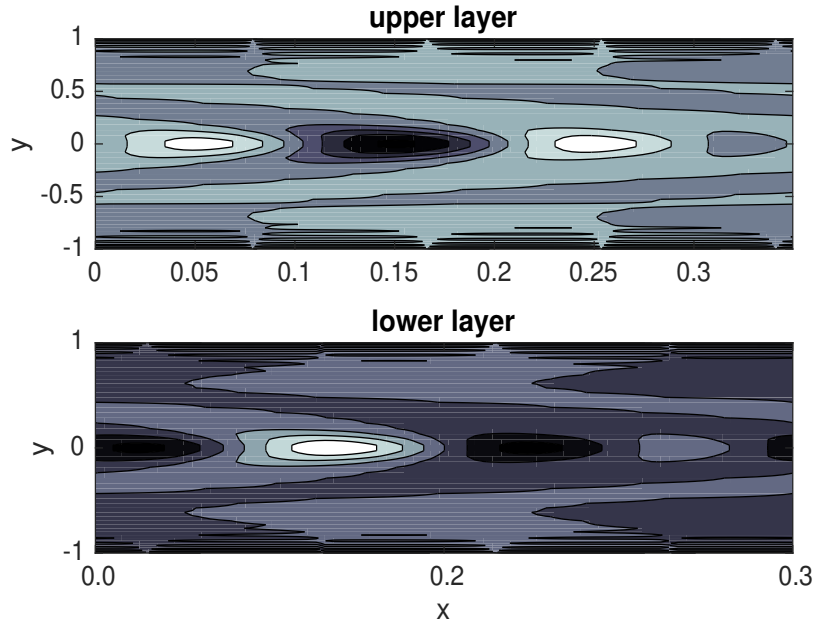


FIGURE 12. Real part of the upper and lower layers of the time quasi-periodic solution ψ_{qp} given in [Theorem 3.2](#) at $t = 0$ for $k = 1$ and $a = 5.722$ where the first two critical wavenumbers are $m_c = 1$ and $m_c = 2$.

a critical threshold Ψ_c . Moreover, as this critical threshold is exceeded, generically a Hopf bifurcation occurs; see [Theorem 3.1](#). To derive this result, we approached the problem by means of dynamic transition theory determining all the attractors near the onset of instability. These attractors then describe how the onset of linear instability translates into the emergence of nonlinear patterns for the actual flow; see [\(3.10\)](#).

Our approach allows for computing the coefficients of the Hopf reduced equation [\(3.9\)](#) by means of explicit formulas involving the interactions between the critical mode and the (zonal) stable ones through the nonlinear terms; see [\(A.8\)-\(A.10\)](#). A numerical examination of these coefficients reveals that instead of infinitely many (stable) modes which would affect the type of transition (supercritical vs subcritical Hopf), the transition is in fact determined by the interactions between the conjugate pair of critical modes losing stability and only the first few zonally homogeneous ($m = 0$) modes. That the interactions with the zonal-mean modes are the determining factors governing the flow patterns emerging after the onset of instability may be viewed as consistent with other works that have shown (in more turbulent regimes) that baroclinic turbulence statistics can be well recovered for certain geophysical flows by omitting the effects of the interactions among the higher-order modes (eddy-eddy interactions); see e.g. [\[24, 23, 33, 9\]](#).

We also investigated the double Hopf bifurcation scenario which takes place at critical length scales where four modes with consecutive wavenumbers become critical. By a rigorous center manifold analysis, we obtain the coefficients of the 4D-ODE system. Our results show that for the parameters we have considered, there exists a quasi-periodic solution that bifurcates. This quasi-periodic solution is a linear combination of two periodic solutions and may be stable depending on the parameters; see [Section 3.3](#). From a transition point of view, in the double Hopf transition, an attractor homeomorphic to 3D sphere bifurcates; see [Theorem 3.2](#). This attractor contains stable/unstable limit cycles and an stable/unstable invariant torus (supporting a quasi-periodic solution).

Overall, our results add more details to the nonlinear development of baroclinic instabilities on a non-constant parallel zonal jet, in that the periodic solutions can become unstable to torus bifurcations and give rise to quasi-periodic behavior. Such a scenario was also found for the barotropic double gyre flow [\[38\]](#), but only in a weakly nonlinear framework using a set of (reduced) amplitude equations. The transition scenario found for the zonally

periodic zonal jet is likely to be more relevant for the ocean circulation than the sideband instabilities in the zonally unbounded zonal jet case which require a nearby band of wavenumbers to be unstable.

In our set-up, the linear friction coefficient in the upper layer is relatively large and as explained needed to balance the vorticity input by the wind stress for generating the zonal jet. When this friction is decreased, more modes will become unstable near the critical point and their interactions are expected to give a detailed view on the development of the unstable modes into ocean vortices, or eddies, due to baroclinic instabilities. In that respect, the dynamic transition theory adopted here, along with extensions based on the variational approach of [6, 5] and its stochastic rectification [7] to handle regimes beyond the onset of instability, provides a way forward to develop a mathematical theory of such ocean-eddy formation processes. The results derived here combined with recent advances in the rigorous analysis of transitions arising in stochastically driven flows [8] open new prospects for the study of regime transitions in stochastically forced ocean models [34, 29].

APPENDIX A. PROOF OF LEMMA 3.1 AND THEOREM 3.1

We first proceed with the proof of Lemma 3.1 For this, we denote the adjoint modes by

$$\psi_{m,j}^* = e^{i\alpha_m x} Y_m^*(y).$$

We denote the critical eigenmode and the critical eigenvalue by

$$\psi_c = \psi_{m_c,1}, \quad \sigma_c = \sigma_{m_c,1}.$$

We denote the bilinear operator \mathcal{G} as

$$\mathcal{G}(u) = G_2(u, u)$$

where $G_2(u, v)$ is linear in each component. Let us define now

$$(A.1) \quad G_s(u, v) = G_2(u, v) + G_2(v, u).$$

The center part of the solution is

$$(A.2) \quad u_c = z(t)\psi_c + c.c.$$

where c.c. stands for complex conjugate of the terms before.

The evolution of $z(t)$ near the onset of transition is obtained by the projection onto the critical mode ψ_c .

$$(A.3) \quad \dot{z} = \sigma_c z + \frac{1}{\langle \mathcal{M}\psi_c, \psi_c^* \rangle} \langle \mathcal{G}(u_c + \Phi), \psi_c^* \rangle.$$

where Φ is the center manifold function. We will obtain its quadratic approximation Φ_2 given by

$$\Phi = \Phi_2(z, \bar{z}) + o(2)$$

Here

$$o(n) = o(|(z, \bar{z})|^n)$$

denotes higher than n -th order terms in z, \bar{z} .

Using the notation (A.1), the reduced equation (A.3) can be written

$$(A.4) \quad \dot{z} = \sigma_c z + \frac{1}{\langle \mathcal{M}\psi_c, \psi_c^* \rangle} \langle G_s(u_c, \Phi_2), \psi_c^* \rangle + o(3).$$

To obtain a closed system, we need to approximate the center manifold function. The approximation of the center manifold in this case reads, see [30],

$$(A.5) \quad \Phi_2 = (2\sigma_c - \mathcal{L})^{-1} \Pi_s G_2(z\psi_c, z\psi_c) + (\sigma_c + \bar{\sigma}_c - \mathcal{L})^{-1} \Pi_s G_2(z\psi_c, \overline{z\psi_c}) + c.c.$$

where $\mathcal{L} = \Pi_s \mathcal{M}^{-1} \mathcal{N}$ and Π_s is the projection on the stable space. Using the formula (A.5), we obtain the following expansion of the center manifold (see also [5, Theorem 2])

$$(A.6) \quad \Phi_2 = z^2 \sum_{j \geq 1} g_{2m_c, j} \psi_{2m_c, j} + |z|^2 \sum_{j \geq 1} g_{0, j} \psi_{0, j} + c.c.$$

Here

$$(A.7) \quad \begin{aligned} g_{0,j} &= \frac{1}{(\sigma_c + \bar{\sigma}_c - \sigma_{0,j}) \langle \mathcal{M} \psi_{0,j}, \psi_{0,j}^* \rangle} \langle G_2(\psi_c, \bar{\psi}_c), \psi_{0,j}^* \rangle \\ g_{2m_c,j} &= \frac{1}{(2\sigma_c - \sigma_{2m_c,j}) \langle \mathcal{M} \psi_{2m_c,j}, \psi_{2m_c,j}^* \rangle} \langle G_2(\psi_c, \psi_c), \psi_{2m_c,j}^* \rangle, \end{aligned}$$

are the coefficients of the center manifold function.

We write (A.4) as (3.9), that is

$$\dot{z} = \sigma_c z + Pz|z|^2 + o(3).$$

which finishes the proof of Lemma 3.1.

Recalling the definition of G_s given in (A.1), the transition number P can then be written as

$$(A.8) \quad P = P_0 + P_2,$$

where

$$(A.9) \quad P_0 = \sum_{j \geq 1} P_{0,j}, \quad P_{0,j} = \frac{1}{\langle \mathcal{M} \psi_c, \psi_c^* \rangle} (g_{0,j} + c.c.) \langle G_s(\psi_c, \psi_{0,j}), \psi_c^* \rangle,$$

denotes the contribution of the zero-wavenumber (stable) modes $\psi_{0,j}$ while

$$(A.10) \quad P_2 = \sum_{j \geq 1} P_{2,j}, \quad P_{2,j} = \frac{1}{\langle \mathcal{M} \psi_c, \psi_c^* \rangle} g_{2m_c,j} \langle G_s(\bar{\psi}_c, \psi_{2m_c,j}), \psi_c^* \rangle,$$

denotes the contribution of the modes $\psi_{2m_c,j}$ on the transition number respectively. The transition type depends on the real part of the transition number P . The proof of Theorem 3.1 follows from the standard Hopf bifurcation analysis of the reduced equation.

APPENDIX B. PROOF OF LEMMA 3.2 AND THEOREM 3.2

As the reduction in the case of (3.8) is similar to the case of (3.7) given in the previous section, we will only mention the differences between these two cases. Under the assumption (3.8), we write the center part of the solution as

$$u_c = z_1(t)\psi_1 + z_2(t)\psi_2 + c.c.$$

where the first two critical modes are

$$\psi_1 = \psi_{m_c,1}, \quad \psi_2 = \psi_{m_c+1,1}, \quad \psi_{-1} = \psi_{-m_c,1}, \quad \psi_{-2} = \psi_{-m_c-1,1}.$$

with corresponding eigenvalues

$$\sigma_1 = \sigma_{m_c,1}, \quad \sigma_2 = \sigma_{m_c+1,1}, \quad \sigma_{-1} = \sigma_{-m_c,1}, \quad \sigma_{-2} = \sigma_{-m_c-1,1}$$

The equation (A.4) becomes the system

$$(B.1) \quad \dot{z}_j = \sigma_j z_j + \frac{1}{\langle \mathcal{M} \psi_j, \psi_j^* \rangle} \langle \mathcal{G}(u_c + \Phi_2), \psi_j^* \rangle + o(3), \quad j = 1, 2.$$

and the center manifold function (A.5) is replaced by

$$\Phi_2 = \sum_{|j|, |k|=1}^2 z_j z_k \Psi_{j,k} + o(2), \quad \Psi_{j,k} = (\sigma_j + \sigma_k - \mathcal{L})^{-1} \Pi_s G_2(\psi_j, \psi_k),$$

where Π_s denotes the projector onto the stable subspace.

Now, the equations (B.1) become (3.11) with the coefficients defined below:

$$\begin{aligned}
A &= g_{1,1,-1,1} + g_{1,-1,1,1} + g_{-1,1,1,1} \\
B &= g_{1,2,-2,1} + g_{1,-2,2,1} + g_{2,1,-2,1} + g_{2,-2,1,1} + g_{-2,1,2,1} + g_{-2,2,1,1} \\
C &= g_{2,1,-1,2} + g_{2,-1,1,2} + g_{1,2,-1,2} + g_{1,-1,2,2} + g_{-1,2,1,2} + g_{-1,1,2,2} \\
D &= g_{2,2,-2,2} + g_{2,-2,2,2} + g_{-2,2,2,2} \\
g_{i,j,k,l} &= \frac{1}{\langle \mathcal{M}\psi_l, \psi_l^* \rangle} \langle G_s(\psi_i, \Psi_{j,k}, \psi_l^*) \rangle, \\
\Psi_{j,k} &= (\sigma_j + \sigma_k - \mathcal{L})^{-1} \Pi_s G_2(\psi_j, \psi_k)
\end{aligned}
\tag{B.2}$$

We note that the above coefficients contain only $g_{i,j,k,l}$ for which $i + j + k = l$. The expansion of the center manifold coefficients can be written more explicitly as (see also [5, Theorem 2])

$$\Psi_{j,k} = \sum_{i=1}^{\infty} \frac{\langle G_2(\psi_{m_j}, \psi_{m_k}), \psi_{m_j+m_k}^* \rangle}{\langle \mathcal{M}\psi_{m_j+m_k}, \psi_{m_j+m_k}^* \rangle} (\sigma_j + \sigma_k - \sigma_{m_j+m_k})^{-1} \psi_{m_j+m_k, i}$$

Now we analyze the equations (3.11) by first putting them in polar form

$$z_j = \rho_j e^{i\gamma_j}, \quad j = 1, 2$$

which yields

$$\begin{aligned}
\dot{\rho}_1 &= \operatorname{Re}(\sigma_1)\rho_1 + \rho_1(\operatorname{Re}(A)\rho_1^2 + \operatorname{Re}(B)\rho_2^2) + \text{h.o.t.} \\
\dot{\rho}_2 &= \operatorname{Re}(\sigma_2)\rho_2 + \rho_2(\operatorname{Re}(C)\rho_1^2 + \operatorname{Re}(D)\rho_2^2) + \text{h.o.t.}
\end{aligned}
\tag{B.3}$$

and

$$\begin{aligned}
\dot{\gamma}_1 &= \operatorname{Im}(\sigma_1) + \text{h.o.t.} \\
\dot{\gamma}_2 &= \operatorname{Im}(\sigma_2) + \text{h.o.t.}
\end{aligned}$$

For the specific case of (3.12), the equations (B.3) always admit the solutions which represent the periodic solutions

$$\begin{aligned}
(\rho_1, \rho_2) &= \left(-\frac{\operatorname{Re}(\sigma_1)}{\operatorname{Re}(A)}, 0 \right), \\
(\rho_1, \rho_2) &= \left(0, -\frac{\operatorname{Re}(\sigma_2)}{\operatorname{Re}(D)} \right),
\end{aligned}$$

with respective eigenvalues

$$\begin{aligned}
\kappa_1 &= -2\sigma_1, & \kappa_2 &= \sigma_2 - \delta\sigma_1 \\
\kappa_1 &= -2\sigma_2, & \kappa_2 &= \sigma_1 - \theta\sigma_2
\end{aligned}$$

Also, the equations (B.3) admit the following solution which represents a quasi-periodic solution

$$(\rho_1, \rho_2) = \left(\frac{\sigma_1 - \theta\sigma_2}{\operatorname{Re}(A)(\theta\delta - 1)}, \frac{\sigma_2 - \delta\sigma_1}{\operatorname{Re}(D)(\theta\delta - 1)} \right).$$

Since the Jacobian matrix of the right hand side of (B.3) at the quasi-periodic solution has determinant

$$\frac{-4(\sigma_2 - \delta\sigma_1)(\sigma_1 - \theta\sigma_2)}{\theta\delta - 1}.$$

With this information, the transition scenarios summarized in Figure 10 and Figure 11 can be obtained by a standard analysis. To prove the claim on the bifurcation of an S^3 -attractor, we need to prove that $(\rho_1, \rho_2) = (0, 0)$ is locally stable equilibrium of (B.3) at $\Psi = \Psi_c$, that is when $\operatorname{Re}(\sigma_1) = \operatorname{Re}(\sigma_2) = 0$. In this case by assumption (3.12), from (B.3), we can obtain

$$\frac{d}{dt}(\rho_1^2 + \rho_2^2) = \operatorname{Re}(A)\rho_1^4 + (\operatorname{Re}(B) + \operatorname{Re}(C))\rho_1^2\rho_2^2 + \operatorname{Re}(D)\rho_2^4 < 0$$

which proves the claim.

APPENDIX C. NUMERICAL TREATMENT OF THE LINEAR STABILITY PROBLEM

To solve the eigenvalue problem numerically, we first plugin the ansatz

$$(C.1) \quad \psi(x, y) = e^{i\alpha_m x} Y_j(y), \quad j \in \mathbb{N}, m \in \mathbb{Z}, \quad \alpha_m := am\pi.$$

into the eigenvalue problem

$$\sigma \mathcal{M} \psi(x, y) = \mathcal{N}(y) \psi(x, y),$$

to obtain

$$(C.2) \quad \sigma \widetilde{\mathcal{M}} Y(y) = \widetilde{\mathcal{N}}(y) Y(y), \quad Y(y) = (Y_1(y), Y_2(y))$$

Here the linear operators $\widetilde{\mathcal{M}}$ and $\widetilde{\mathcal{N}}(y)$ are defined as

$$(C.3) \quad \widetilde{\mathcal{M}} = \begin{bmatrix} \Delta_m - F_1 & F_1 \\ F_2 & \Delta_m - F_2 \end{bmatrix}, \quad \widetilde{\mathcal{N}}(y) = \begin{bmatrix} N_{11} & N_{12} \\ N_{21} & N_{22} \end{bmatrix}$$

where

$$(C.4) \quad \begin{aligned} N_{11} &= c_1 \cos k\pi y ((k\pi)^2 + \Delta_m) - \beta i \alpha_m - r_1 \Delta_m \\ N_{12} &= c_1 F_1 \cos k\pi y \\ N_{21} &= 0 \\ N_{22} &= -c_1 F_2 \cos k\pi y - \beta i \alpha_m - r_2 \Delta_m \\ \Delta_m &= D^2 - \alpha_m^2, \quad D = \frac{\partial}{\partial y} \\ c_1 &= \Psi k \pi i \alpha_m. \end{aligned}$$

The eigenvalue problem (C.2) is supplemented with the following boundary conditions

$$(C.5) \quad Y_i(\pm 1) = D^2 Y_i(\pm 1) = 0, \quad i = 1, 2.$$

We use Legendre-Galerkin method to discretize and solve the (C.2) with boundary conditions (C.5). We refer to [31] for the details of the Legendre-Galerkin method and to [10] for its use in dynamical transition problems.

Let $\{L_j\}$ be the Legendre polynomials and consider compact combinations of the Legendre polynomials

$$f_j(y) = L_j(y) + \sum_{k=1}^4 c_{jk} L_{j+k}(y)$$

with c_{jk} chosen so that f_j satisfy the boundary conditions (C.5), i.e.

$$f_j(\pm 1) = D^2 f_j(\pm 1) = 0.$$

To discretize the eigenvalue problem, we plug

$$(C.6) \quad Y_i^{N_y}(y) = \sum_{j=0}^{N_y-1} y_j^{(i)} f_j(y), \quad \widehat{Y}_i = [y_0^{(i)}, \dots, y_{N_y-1}^{(i)}]^T, \quad i = 1, 2.$$

into (C.2) to obtain

$$(C.7) \quad \sigma \begin{bmatrix} \widehat{\Delta}_m - F_1 A_3 & F_1 A_3 \\ F_2 A_3 & \widehat{\Delta}_m - F_2 A_3 \end{bmatrix} \begin{bmatrix} \widehat{Y}_1 \\ \widehat{Y}_2 \end{bmatrix} = \begin{bmatrix} \widehat{N}_{11} & \widehat{N}_{12} \\ \widehat{N}_{21} & \widehat{N}_{22} \end{bmatrix} \begin{bmatrix} \widehat{Y}_1 \\ \widehat{Y}_2 \end{bmatrix}$$

$$(C.8) \quad \begin{aligned} \widehat{N}_{11} &= c_1 (k\pi)^2 A_5 + c_1 (A_4^T - \alpha_m^2 A_5) - \beta i \alpha_m A_3 - r_1 \widehat{\Delta}_m \\ \widehat{N}_{12} &= c_1 F_1 A_5 \\ \widehat{N}_{21} &= 0 \\ \widehat{N}_{22} &= -c_1 F_2 A_5 - \beta i \alpha_m A_3 - r_2 \widehat{\Delta}_m \end{aligned}$$

Here

$$(C.9) \quad \begin{aligned} A_1 &= (D^4 f_j, f_k), & A_2 &= (D^2 f_j, f_k), & A_3 &= (f_j, f_k), \\ A_4 &= (\cos k\pi y D^2 f_j, f_k), & A_5 &= (\cos k\pi y f_j, f_k), \\ \widehat{\Delta}_m &= A_2 - \alpha_m^2 A_3, \end{aligned}$$

with $(f, g) = \int_{-1}^1 f(y)g(y) dy$. The explicit expression of the matrices A_i , $i = 1, \dots, 5$ can be found in [10].

APPENDIX D. PRACTICAL ASPECTS FOR THE CALCULATION OF THE TRANSITION NUMBER

The practical calculation of the P_0 -term in (A.9) and the P_2 -term in (A.10), boils down to the efficient calculation of the inner and trilinear products involved therein. In that respect, we provide here explicit expressions of the latter. They are given by

$$\begin{aligned} \langle \mathcal{M}\psi_{m,j}, \psi_{m,j}^* \rangle &= i\alpha_m \int_{-1}^1 ((D^2 - \alpha_m^2 - F_1)Y_{m,j}^1 + F_1 D Y_{m,j}^2) \overline{Y_{m,j}^{*1}} dy \\ &\quad + i\alpha_m \int_{-1}^1 ((D^2 - \alpha_m^2 - F_2)Y_{m,j}^2 + F_2 D Y_{m,j}^1) \overline{Y_{m,j}^{*2}} dy, \end{aligned}$$

and

$$\langle G_2(\psi_{m,j}, \psi_{n,k}), \psi_{p,l}^* \rangle = -\delta_{m+n-p} \left(\int_{-1}^1 G_2^1 \overline{Y_{p,l}^{*1}} + G_2^2 \overline{Y_{p,l}^{*2}} \right) dy,$$

$$\begin{aligned} G_2^1 &= i\alpha_m Y_{m,j}^1 (D(D^2 - \alpha_n^2 - F_1)Y_{n,k}^1 + F_1 D Y_{n,k}^2) \\ &\quad - i\alpha_n ((D^2 - \alpha_n^2 - F_1)Y_{n,k}^1 + F_1 Y_{n,k}^2) D Y_{m,j}^1 \\ G_2^2 &= i\alpha_m Y_{m,j}^2 (D(D^2 - \alpha_n^2 - F_2)Y_{n,k}^2 + F_2 D Y_{n,k}^1) \\ &\quad - i\alpha_n ((D^2 - \alpha_n^2 - F_2)Y_{n,k}^2 + F_2 Y_{n,k}^1) D Y_{m,j}^2. \end{aligned}$$

In practice, the integrals can be evaluated by any commonly used quadrature rules in which the values of the integrand are evaluated at quadrature points. In our calculations, we use

$$\int_{-1}^1 f(y) dy = \sum_{n=0}^{N_y} f(y_n) \omega_n,$$

where y_n and ω_n are Legendre-Gauss-Lobatto quadrature points and weights respectively.

APPENDIX E. MODEL PARAMETERS

L_y	meridional length scale	10^6 m
H_1	upper layer depth	250m
H_2	upper layer depth	750m
$\Delta\rho$	density difference	$\rho_2 - \rho_1 = 1 \text{ kgm}^{-3}$
U	characteristic velocity	$\tau_0/(\rho_0 H_1 \beta_0 L_y) = 0.02 \text{ m s}^{-1}$
τ_0	characteristic zonal wind stress	0.1 Pa
β_0	planetary vorticity gradient	$2 \times 10^{-11} \text{ (ms)}^{-1}$
f_0	reference Coriolis parameter	10^{-4} s^{-1}
ϵ_0	bottom friction coefficient	10^{-7} s^{-1}
g	gravitational acceleration	9.8 ms^{-2}
g'	reduced gravity	$g\Delta\rho/\rho_0 = 0.01 \text{ ms}^{-2}$
ρ_0	reference density	10^3 kgm^{-3}
F_1	upper layer Froude number	$f_0^2 L_y^2 / (g' H_1) = 4000$
F_2	lower layer Froude number	$f_0^2 L_y^2 / (g' H_2) = 4000/3$
β	planetary vorticity factor	$\beta_0 L_y^2 / U = 1000$
τ	wind-stress parameter	1.0
r_2	lower layer linear friction coefficient	$r_2 = \epsilon_0 L_y / U = 5.0$

TABLE 2. Set of model parameters used in the numerical study of the problem.

Acknowledgments: The authors are grateful for two anonymous reviewers for their insightful comments.

This work has been partially supported by the European Research Council (ERC) under the European Union’s Horizon 2020 research and innovation program (grant agreement No. 810370). This study was also supported by a Ben May Center grant for theoretical and/or computational research and by the Office of Naval Research Multidisciplinary University Research Initiative Grant N00014-20- 1-2023.

REFERENCES

- [1] Bernier, C.: Existence of attractor for the quasi-geostrophic approximation of the Navier-Stokes equations and estimate of its dimension. *Adv. Math. Sci. Appl.* (4), 465–489 (1994)
- [2] Brézis, H.: *Functional Analysis, Sobolev Spaces and Partial Differential Equations*. Springer (2010)
- [3] Cai, M., Hernandez, M., Ong, K., Wang, S.: Baroclinic instability and transitions in a two-layer quasigeostrophic channel model. *arXiv:1705.07989 [physics]* (2017)
- [4] Chekroun, M.D., Koren, I., Liu, H.: Efficient reduction for diagnosing Hopf bifurcation in delay differential systems: Applications to cloud-rain models. *Chaos (Woodbury, N.Y.)* **30**(5), 053130 (2020)
- [5] Chekroun, M.D., Liu, H., McWilliams, J.: Variational approach to closure of nonlinear dynamical systems: Autonomous case. *Journal of Statistical Physics* **179**(5), 1073–1160 (2020)
- [6] Chekroun, M.D., Liu, H., McWilliams, J.C.: The emergence of fast oscillations in a reduced primitive equation model and its implications for closure theories. *Comp. & Fluids* **151**, 3–22 (2017).
- [7] Chekroun, M.D., Liu, H., McWilliams, J.C.: Stochastic rectification of fast oscillations on slow manifold closures. *Proc. Natl. Acad. Sci. USA* **118**(48), e2113650118 (2021)
- [8] Chekroun, M.D., Liu, H., McWilliams, J.C., Wang, S.: Transitions in stochastic non-equilibrium systems: Efficient reduction and analysis. *arXiv preprint arXiv:2202.07031* (2022)
- [9] Chemke, R., Kaspi, Y.: The effect of eddy–eddy interactions on jet formation and macroturbulent scales. *J. Atmos. Sci.* **73**(5), 2049–2059 (2016)

- [10] Dijkstra, H., Sengul, T., Shen, J., Wang, S.: Dynamic transitions of quasi-geostrophic channel flow. *SIAM Journal on Applied Mathematics* **75**(5), 2361–2378 (2015).
- [11] Dijkstra, H.A.: *Nonlinear Physical Oceanography: A Dynamical Systems Approach to the Large Scale Ocean Circulation and El Niño*, second edn. Springer, New York, 532 pp. (2005)
- [12] Dijkstra, H.A., Katsman, C.A.: Temporal variability of the wind-driven quasi-geostrophic double gyre ocean circulation: Basic bifurcation diagrams. *Geophys. Astrophys. Fluid Dyn.* **85**, 195–232 (1997)
- [13] Dijkstra, H.A., Van der Vaart, P. C. F.: On the physics of upgradient momentum transport in unstable eastward jets. *Geophys. Astrophys. Fluid Dyn.* **88**, 295–323 (1998)
- [14] Eady, E.T.: Long waves and cyclone waves. *Tellus* **1**, 33–52 (1949)
- [15] Kieu, C., Sengul, T., Wang, Q., Yan, D.: On the Hopf (double Hopf) bifurcations and transitions of two-layer western boundary currents. *Communications in Nonlinear Science and Numerical Simulation* **65**, 196–215 (2018).
- [16] Kuznetsov, Y.: *Elements of Applied Bifurcation Theory*, third edn. Applied Mathematical Sciences. Springer-Verlag, New York (2004).
- [17] Li, K.: Dynamic transitions of the Swift-Hohenberg equation with third-order dispersion. *Discrete & Continuous Dynamical Systems - B* (2020).
- [18] Lovegrove, A.F., Moroz, I.M., Read, P.L.: Bifurcations and instabilities in rotating, two-layer fluids: II. β -Plane. *Nonlinear Processes in Geophysics* **9**(3/4), 289–309 (2002).
- [19] Lu, C., Mao, Y., Sengul, T., Wang, Q.: On the spectral instability and bifurcation of the 2d-quasi-geostrophic potential vorticity equation with a generalized Kolmogorov forcing. *Physica D: Nonlinear Phenomena* **403**, 132296 (2020).
- [20] Ma, T., Wang, S.: *Bifurcation Theory and Applications*, *World Scientific Series on Nonlinear Science Series A*, vol. 53. World Scientific (2005).
- [21] Ma, T., Wang, S.: *Phase Transition Dynamics*. Springer International Publishing, Cham (2019).
- [22] Meshalkin, L.D., Sinai, I.G.: Investigation of the stability of a stationary solution of a system of equations for the plane movement of an incompressible viscous liquid. *Journal of Applied Mathematics and Mechanics* **25**(6), 1700–1705 (1961).
- [23] O’Gorman, P.A., Schneider, T.: Recovery of atmospheric flow statistics in a general circulation model without nonlinear eddy-eddy interactions. *Geophysical Research Letters* **34**(22) (2007).
- [24] Panetta, R., Held, I.: Baroclinic eddy fluxes in a one-dimensional model of quasi-geostrophic turbulence. *J. Atmos. Sci.* **45**(22), 3354–3365 (1988)
- [25] Pedlosky, J.: Finite-amplitude baroclinic waves. *Journal of the Atmospheric Sciences* **27**(1), 15–30 (1970).
- [26] Pedlosky, J.: *Geophysical Fluid Dynamics*, second edn. Springer-Verlag, New York (1987)
- [27] Phillips, N.A.: A simple three-dimensional model for the study of large-scale extratropical flow patterns. *J. Meteor.* **8**, 381–394 (1951)
- [28] Romea, R.D.: The effects of friction and β on finite amplitude baroclinic waves. *Journal of Atmospheric Science* **34**, 1689–1695 (1977)
- [29] Sapsis, T.P., Dijkstra, H.A.: Interaction of additive noise and nonlinear dynamics in the double-gyre wind-driven ocean circulation. *Journal of physical oceanography* **43**(2), 366–381 (2013)
- [30] Şengül, T., Wang, S.: Dynamic transitions and baroclinic instability for 3d continuously stratified Boussinesq flows. *Journal of Mathematical Fluid Mechanics* **20**(3), 1173–1193 (2018).
- [31] Shen, J., Tang, T., Wang, L.L.: *Spectral Methods*, *Springer Series in Computational Mathematics*, vol. 41. Springer Berlin Heidelberg, Berlin, Heidelberg (2011).
- [32] Simonnet, E., Ghil, M., Wang, S., Chen, Z.M.: Hopf bifurcation in quasi-geostrophic channel flow. *SIAM Journal on Applied Mathematics* **64**(1), 343–368 (2003)
- [33] Srinivasan, K., Young, W.: Zonostrophic instability. *J. Atmos. Sci.* **69**(5), 1633–1656 (2012)
- [34] Sura, P., Fraedrich, K., Lunkeit, F.: Regime transitions in a stochastically forced double-gyre model. *Journal of Physical Oceanography* **31**(2), 411–426 (2001)
- [35] Talley, L.: *Descriptive Physical Oceanography*. Academic Press, New York (2011)
- [36] Vallis, G.: *Atmospheric and Oceanic Fluid Dynamics*. Cambridge University Press, Cambridge, UK (2006)
- [37] Van der Vaart, P.C.F., Dijkstra, H.A.: Sideband instabilities of mixed barotropic/baroclinic waves growing on a midlatitude zonal jet. *Physics of Fluids* **9**, 615–631 (1997)
- [38] Van der Vaart, P. C. F., Schuttelaars, H.M., Calvete, D., Dijkstra, H.A.: Instability of time-dependent wind-driven ocean gyres. *Physics of Fluids* **14**, 3601–3615 (2002)
- [39] Welander, P.: A two-layer frictional model of wind-driven motion in a rectangular oceanic basin. *Tellus* **18**(1), 54–62 (1966).

(Chekroun) DEPARTMENT OF EARTH AND PLANETARY SCIENCES, WEIZMANN INSTITUTE, REHOVOT 76100, ISRAEL
Email address: michael-david.chekroun@weizmann.ac.il

(Dijkstra) CENTRE FOR COMPLEX SYSTEM STUDIES, DEPARTMENT OF PHYSICS, UTRECHT UNIVERSITY, UTRECHT, THE NETHERLANDS
Email address: h.a.dijkstra@uu.nl

(Şengül) DEPARTMENT OF MATHEMATICS, MARMARA UNIVERSITY, 34722 ISTANBUL, TURKEY
Email address: taylan.sengul@marmara.edu.tr

(Wang) DEPARTMENT OF MATHEMATICS, INDIANA UNIVERSITY, BLOOMINGTON, IN 47405
Email address: showang@indiana.edu, <http://www.indiana.edu/~fluid>